Moving Vortices on the Sphere: A Test Case for Horizontal Advection Problems

RAMACHANDRAN D. NAIR

Computational Mathematics Group, Institute for Mathematics Applied to Geosciences, National Center for Atmospheric Research,* Boulder, Colorado

CHRISTIANE JABLONOWSKI

Department of Atmospheric, Oceanic, and Space Sciences, University of Michigan, Ann Arbor, Michigan

ABSTRACT

A new two-dimensional advection test on the surface of the sphere is proposed. The test combines a solid-body rotation and a deformational flow field to form moving vortices over the surface of the sphere. The resulting time-dependent deforming vortex centers are located on diametrically opposite sides of the sphere and move along a predetermined great circle trajectory. The horizontal wind field is deformational and nondivergent, and the analytic solution is known at any time. During one revolution around the sphere the initially smooth transported scalar develops strong gradients. Such an approach is therefore more challenging than existing advection test cases on the sphere. To demonstrate the effectiveness and versatility of the proposed test, three different advection schemes are employed, such as a discontinuous Galerkin method on a cubed-sphere mesh, a classical semi-Lagrangian method, and a finite-volume algorithm with adaptive mesh refinement (AMR) on a regular latitude–longitude grid. The numerical results are compared with the analytic solution for different flow orientation angles on the sphere.

1. Introduction

The two-dimensional horizontal advection tests on the surface of a sphere may be classified into two groups: solid-body rotation tests and deformational flow tests. Williamson et al. (1992, hereinafter W92) standardized the solid-body rotation test on the sphere based on the earlier works of Ritchie (1987) and Williamson and Rasch (1989). This test is especially designed to evaluate the numerical schemes used for the horizontal advection in a nondivergent wind field and is the most widely used advection test case in spherical geometry. For the solid-body rotation test, the exact solution is known and the flow orientation is controlled by a parameter. Therefore, the underlying advection

scheme can be evaluated at a region of particular interest, for example, the polar regions of the latitude–longitude geometry or the vertices and edges of the cubed-sphere geometry (Nair et al. 2005). W92 used a "cosine bell" (a C^1 function) as the advected scalar field. However, for a rigorous monotonicity test the field may be chosen to be a nonsmooth scalar such as a square block (Williamson and Rasch 1989) or a slotted cylinder (Nair et al. 2003; Lipscomb and Ringler 2005; Jablonowski et al. 2006).

There are only a few choices for the deformational flow test on the sphere with known analytic solutions. An example is the nondivergent vortex (idealized cyclogenesis) problem first proposed by Doswell (1984) that was extended to spherical geometry by Nair et al. (1999). In particular, Nair et al. (1999) used a polar stereographic plane tangent to the north pole of a rotated coordinate system to define the deforming vortex. The parameters were chosen to make the vortex nonsmooth. The vortex center is stationary with a strong deformational flow field. Because of the evolving sharp gradients, this test is more challenging than the solid-body rotation test. Nair and Machenhauer (2002) fur-

ther extended this problem without using a tangent plane and introduced two vortices located on diametrically opposite sides of a sphere. These deformational test cases are becoming popular for evaluating new advection schemes on the sphere (e.g., Zerroukat et al. 2004; Peng et al. 2006; Flyer and Wright 2007) and adaptive mesh refinement (AMR) applications (Hubbard and Nikiforakis 2003; Jablonowski et al. 2006).

In this paper we propose a new advection test on the sphere, which has the components from the deformational flow and solid-body rotation tests. The test introduces moving vortices on the sphere and is based on the deformational flow test case considered in Nair and Machenhauer (2002). The vortices are not stationary and move along a predetermined trajectory with a known analytic solution. This allows the computation of error norms that assess the accuracy of the numerical schemes. None of the existing advection test cases is capable of mimicking a nonlocalized evolving field as seen in the atmosphere. However, the proposed test problem is designed to have this feature and poses a challenging test for advection schemes. Here, we demonstrate the characteristics of the moving vortex test case with three very different advection schemes that are extracted out of existing shallow-water models. These are a discontinuous Galerkin advection method on a cubed-sphere grid (Nair et al. 2005), a classical semi-Lagrangian advection technique (Nair et al. 2003), and a finite-volume algorithm with AMR on a regular latitude–longitude grid (Jablonowski et al. 2006).

The paper is organized as follows: Section 2 introduces the concept of rotated coordinate systems, followed by a description of the 2D advection problem on the sphere. In addition, the existing solid-body rotation and deformational flow tests are reviewed. The new moving vortex test case is introduced in section 3. In particular, the section explains the composition of the translating and rotating wind field, the analytic solution of the advected scalar, and the computation of the departure points for semi-Lagrangian schemes. In section 4, we present results of the moving vortex test for the three advection algorithms. These highlight the application areas of the new test and serve as a point of reference for future model intercomparisons. Section 5 provides the summary and conclusions.

2. Rotational motion on the sphere

To develop idealized advection tests, we utilize a rotated spherical coordinate system that is offset with respect to the regular spherical coordinate system. Consider a sphere with radius a whose surface is defined by
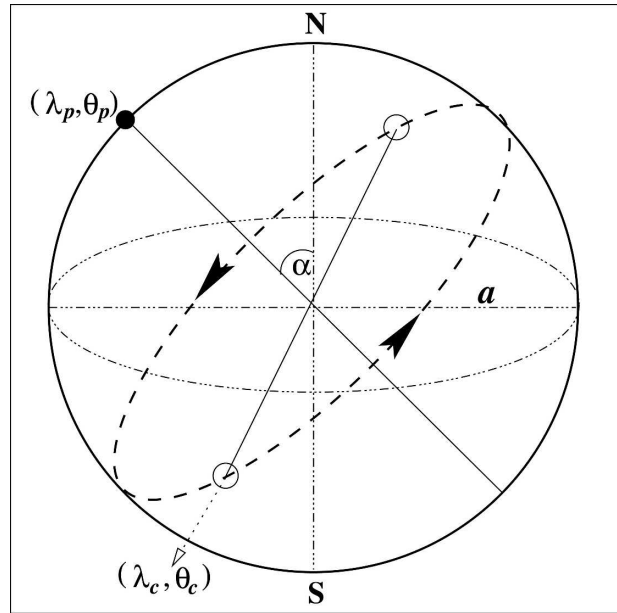

FIG. 1. Schematic positions of the vortices (small open circles) on the equator of a rotated coordinate system (λ', θ') whose north pole is at (λ_p, θ_p) with respect to the regular (λ, θ) sphere with radius a. A vortex center is denoted by (λ_c, θ_c), and α is the angle between the axis of solid-body rotation and the polar axis of spherical coordinate system (flow-orientation parameter).

the spherical coordinates (λ, θ), where λ and θ are the longitude and latitude, respectively. Then the components of the velocity vector $\mathbf{v} = (u, v)$ along the east and north directions, respectively, are defined by

$$u = a \cos\theta \frac{d\lambda}{dt} \quad \text{and} \tag{1}$$

$$v = a \frac{d\theta}{dt}. \tag{2}$$

To derive the analytic velocity field, we consider a rotated coordinate system (λ', θ'), which has the north pole at (λ_p, θ_p) with respect to the unrotated (λ, θ) coordinate system (see Fig. 1). The velocity fields (u, v) can be specified in terms of the rotational motion of the (λ', θ') sphere as described below.

Define the angular velocity in (λ', θ') to be (Ritchie 1987)

$$\frac{d\lambda'}{dt} \equiv \omega \quad \text{and} \tag{3}$$

$$\frac{d\theta'}{dt} \equiv 0. \tag{4}$$

The spherical trigonometric relations between these two coordinate systems are then given by

$$\sin\theta' = \sin\theta \sin\theta_p + \cos\theta \cos\theta_p \cos(\lambda - \lambda_p), \qquad (5)$$

$$\sin\theta = \sin\theta' \sin\theta_p - \cos\theta' \cos\theta_p \cos\lambda', \quad \text{and} \qquad (6)$$

$$\cos\theta \sin(\lambda - \lambda_p) = \cos\theta' \sin\lambda'. \qquad (7)$$

For any known position of the north pole (λ_p, θ_p), the unrotated coordinates (λ, θ) can be specified in terms of the rotated coordinates (λ', θ') by employing Eqs. (5)–(7) such that

$$\lambda'(\lambda, \theta) = \arctan\left[\frac{\cos\theta \sin(\lambda - \lambda_p)}{\cos\theta \sin\theta_p \cos(\lambda - \lambda_p) - \cos\theta_p \sin\theta}\right] \qquad (8)$$

and

$$\theta'(\lambda, \theta) = \arcsin[\sin\theta \sin\theta_p + \cos\theta \cos\theta_p \cos(\lambda - \lambda_p)]. \qquad (9)$$

The corresponding inverse relations can then be derived as

$$\lambda(\lambda', \theta') = \lambda_p + \arctan\left(\frac{\cos\theta' \sin\lambda'}{\sin\theta' \cos\theta_p + \cos\theta' \cos\lambda' \sin\theta_p}\right) \qquad (10)$$

and

$$\theta(\lambda', \theta') = \arcsin(\sin\theta' \sin\theta_p - \cos\theta' \cos\theta_p \cos\lambda'). \qquad (11)$$

Taking the total time derivative of Eq. (6) and using Eqs. (2)–(4) and (7) yields the the meridional velocity component

$$v = a\omega \cos\theta_p \sin(\lambda - \lambda_p). \qquad (12)$$

Similarly, differentiating Eq. (5) and using Eqs. (1), (2), and (12), the zonal velocity u can be derived as follows:

$$u = a\omega[\sin\theta_p \cos\theta - \cos\theta_p \cos(\lambda - \lambda_p) \sin\theta]. \qquad (13)$$

The angular velocity ω defined in the rotated system is not necessarily a constant. In the special case of the solid-body rotation test discussed later, the corresponding $\omega = \omega_s$ with $u_0 = a\omega_s$ is defined to be a constant (W92). However, for the deformational flow considered in Nair et al. (1999), $\omega = \omega_r$ is dependent on the latitude of the rotated coordinate system $[\omega_r = \omega_r(\theta')]$. We use Eqs. (12) and (13) to formulate the velocity fields for the moving vortices in section 3.

a. Advection (transport) problem on the sphere

Advection problems are a test bed for any numerical scheme considered for global modeling. Numerical techniques based on finite-volume or discontinuous Galerkin methods rely on conservation laws and employ the transport equation in conservation form. Assuming constant density and a nondivergent flow, the conservation law for a transported scalar ϕ (without a source or sink) is given by

$$\frac{\partial\phi}{\partial t} + \boldsymbol{\nabla} \cdot (\mathbf{v}\phi) = 0 \quad \text{in} \quad S \times [0, T], \qquad (14)$$

where S is the surface of the sphere (which is a closed domain without boundaries), $t \in [0, T]$ is the time where T denotes the ending time of the simulation, $(\boldsymbol{\nabla}\cdot)$ symbolizes the horizontal divergence operator (see also W92 for the definition in spherical coordinates), and $\mathbf{v} = (u, v)$ represents the horizontal wind vector with the zonal and meridional velocities u and v. Equation (14) is often referred to as the conservative or flux form of the transport equation. The transport equation in *advective* form is used for many nonconservative numerical methods such as spectral methods. It can be written as

$$\frac{\partial\phi}{\partial t} + \mathbf{v} \cdot \boldsymbol{\nabla}\phi \equiv \frac{D\phi}{Dt} = 0, \qquad (15)$$

where $\boldsymbol{\nabla}$ stands for the horizontal gradient operator and D/Dt is the total (material) time derivative, which is used for semi-Lagrangian modeling.

b. Review of advection test cases

Since the moving vortex problem proposed herein consists of the ideas used in the solid-body rotation as well as the deformational flow problems, we briefly review these test cases in the following section. In particular, we specify initial conditions for the transport equations in Eqs. (14) and (15) for both test problems. This includes defining the spherical velocity vector $\mathbf{v}$ such that the exact solution is known at any given time.

1) SOLID-BODY ROTATION ON THE SPHERE

The velocity field in the solid-body rotation test is controlled by a flow orientation parameter α, which is the angle between the axis of solid-body rotation and the polar axis of spherical coordinate system (W92) as shown in Fig. 1.

By choosing the north pole of the rotated sphere to be $(\lambda_p, \theta_p) = (\pi, \pi/2 - \alpha)$ with respect to the unrotated sphere, and the rotation rate as $a\omega_s = u_0$, the wind components (u_s, v_s) can be written using Eqs. (12) and (13) as follows:

$$u_s = u_0(\cos\theta \cos\alpha + \sin\theta \cos\lambda \sin\alpha) \quad \text{and} \qquad (16)$$

$$v_s = -u_0 \sin\lambda \sin\alpha. \qquad (17)$$

This configuration keeps a uniform flow on the regular sphere along its equatorial, northeast and north–south directions for the parameter values $\alpha = 0°$, $45°$, and $90°$, respectively. The initial scalar field ϕ is a cosine bell centered at the equator of the unrotated sphere. The details of the scalar field $\phi(t = 0)$ are described in W92. After one complete revolution, the cosine bell reaches its initial position such that the analytic solution is exactly the same as the initial conditions $\phi(0) = \phi(T)$. The rotation rate is a constant and given by $u_0 = 2\pi a/$ (12 days) where $a = 6.371\ 229 \times 10^6$ m represents the mean radius of the sphere. Therefore, 12 days of model integration are required to complete one revolution of the transported scalar around the globe.

2) DEFORMATIONAL FLOW TEST (STATIONARY VORTEX)

The deformation test proposed in Nair and Machenhauer (2002) consists of two static vortices located on diametrically opposite sides of the sphere. They are designed in such a way that the centers of the vortices are at the north and south poles of the rotated (λ', θ') sphere.

Since the two vortices are generated symmetrically on the sphere, we only need to consider one vortex for which the center is located at (λ_p, θ_p) with respect to the unrotated sphere. This steady circular vortex is defined to have the normalized tangential velocity $V = (3\sqrt{3}/2)\ \text{sech}^2(\rho)\ \tanh(\rho)$, where $\rho = \rho_0 \cos\theta'$ is the radial distance of the vortex and ρ_0 is a constant parameter. Note that the normalized coefficient $3\sqrt{3}/2$ is obtained by dividing the analytical maximum value of the function $y(x) = \text{sech}^2(x)\tanh(x)$.

Nair and Machenhauer (2002) formulated the deformational problem on a unit sphere with nondimensional space and time parameters. However, here we consider the problem with physical dimensions and parameters that are consistent with those introduced in W92. A scale factor for the tangential velocity V is chosen to be $v_0 = 2\pi a/T$, where T is the total (final) time for the simulation and set to be $T = 12$ days. Thus, the scaled tangential velocity is

$$V = v_0 \frac{3\sqrt{3}}{2} \text{sech}^2(\rho)\ \tanh(\rho). \tag{18}$$

In the rotated (λ', θ') coordinates the components of the vector velocity are defined by Eqs. (3) and (4). However, in the deforming vortex case the angular velocity ω_r varies with the vortex *radial distance, $a\rho$,* and is defined by

$$\omega_r(\theta') = \begin{cases} V/(a\rho) & \text{if } \rho \neq 0, \\ 0 & \text{if } \rho = 0, \end{cases} \tag{19}$$

which has the physical unit of radians seconds^{-1}. When using Eqs. (12) and (13), the velocity components for the deformational flow (u_r, v_r) on the sphere can now be written as

$$u_r = a\omega_r(\theta')[\sin\theta_p \cos\theta - \cos\theta_p \cos(\lambda - \lambda_p)\sin\theta] \quad \text{and} \tag{20}$$

$$v_r = a\omega_r(\theta')[\cos\theta_p \sin(\lambda - \lambda_p)]. \tag{21}$$

Here, (λ_p, θ_p) defines the center of the vortex, which is independent of time in this stationary setup.

The exact solution for ϕ at time t that corresponds to that given in Nair and Machenhauer (2002) on the (λ', θ') sphere for Eqs. (14) or (15) is

$$\phi(\lambda', \theta', t) = 1 - \tanh\left[\frac{\rho}{\gamma}\sin(\lambda' - \omega_r t)\right], \tag{22}$$

where γ is a parameter controlling the "stiffness" of the field (Nair et al. 1999). The initial field is given by $\phi(\lambda', \theta', t = 0)$. For a "smooth" deformational flow, the parameter values $\rho_0 = 3$ and $\gamma = 5$ are chosen. The choice of the vortex center (λ_p, θ_p) on the spherical surface can be made for any area of special interest. These might include the polar regions for models with latitude–longitude grids or one of the corner points of the cube for models in cubed-sphere geometry.

3. Moving vortices on the sphere

a. Composition of the wind field

The wind field for the moving vortices is a combination of wind vectors of the solid-body rotation (u_s, v_s) and that of the deformational flow (u_r, v_r). The solid-body rotation wind serves as a *background* flow for the problem. Let (λ_c, θ_c) be the center of the vortex, which is free to move anywhere on the sphere. Then, the background velocity moves the vortex center $[\lambda_c(t), \theta_c(t)]$ along a trajectory. Note that the position of the vortex center is now time dependent. In addition, the vortex can evolve (deform) with its own velocity (u_r, v_r) while moving along the trajectory. The background wind (u_s, v_s) will not have any effect on the vortex deformation other than translating the entire deformational field uniformly across the sphere.

If we place the center (λ_c, θ_c) on the equator of a rotated sphere in such a way that the parameter α is equal to the angle between the axis of rotation and the polar axis of the unrotated spherical coordinate system (see Fig. 1), then we can direct the motion of the vortex center along a great circle trajectory. Its orientation is controlled by the flow orientation parameter α as in the

case of the solid-body rotation test [see Eqs. (16) and (17)].

Because of the time dependency of the vortex center, the rotational vortex velocities are now expressed by the time-dependent wind speeds $u_r(t)$ and $v_r(t)$. Since both wind vectors (u_s, v_s) and (u_r, v_r) are acting on the same vortex system, they can be combined to form a single wind vector field $\mathbf{v}(t) = [u(t), v(t)]$ at time t for the entire moving vortex. It follows that

$$u(t) = u_s + u_r(t) \quad \text{and} \quad v(t) = v_s + v_r(t). \quad (23)$$

The wind vector $\mathbf{v}(t)$ for the moving vortex using Eqs. (16), (17), (20), and (21) with scaling parameters can be written as

$$u(t) = u_0(\cos\theta \cos\alpha + \sin\theta \cos\lambda \sin\alpha)$$
$$+ a\omega_r\{ \sin\theta_c(t) \cos\theta - \cos\theta_c(t) \cos[\lambda - \lambda_c(t)] \sin\theta\}$$

(24)

and

$$v(t) = -u_0 \sin\lambda \sin\alpha + a\omega_r\{ \cos\theta_c(t) \sin[\lambda - \lambda_c(t)]\}.$$

(25)

For the present study we choose $u_0 = 2\pi a/(12 \text{ days})$, and ω_r is given by Eq. (19). Initially a vortex center is located at $[\lambda_c(t = 0), \theta_c(t = 0)] = (\lambda_0, \theta_0) = (3\pi/2, 0)$; with this setup the other vortex center will be placed at the diametrically opposite point $(\pi/2, 0)$. Thus, the vortices have the initial and final positions (after 12 days, or with one complete revolution) geographically located at 90°E and 90°W on the equator.

From a computational viewpoint, the wind fields in Eqs. (24) and (25) can be generated as follows: The first step is to find the vortex center $[\lambda_c(t), \theta_c(t)]$ as a function of both time and the flow orientation parameter α. Let Δt be the time step such that $t_n = n\Delta t, n = 1, 2, \ldots, N$ where n indicates the number of the current time step and $t_N = T$. For a given α and a time level t_n, the position of the vortex center displaces along the equator of the rotated sphere (λ', θ') and is located at $(\lambda_0' + \omega_s t_n, \theta_0')$. Here, (λ_0', θ_0') is the initial vortex center with respect to the rotated sphere. Practically, this position (i.e., vortex center at a given time) can be obtained in terms of (λ, θ) coordinates by computing (λ_0', θ_0') in the rotated sphere whose north pole is at $(\lambda_p, \theta_p) = (\pi, \pi/2 - \alpha)$ and using Eqs. (8) and (9). Then the position $(\lambda_0' + \omega_s t_n, \theta_0')$ is rotated back to the regular spherical coordinates by using Eqs. (10) and (11). Let $[\lambda_c(t_n), \theta_c(t_n)]$ be the vortex center position at a known time level t_n.

The second step is the generation of the vortex at $[\lambda_c(t_n), \theta_c(t_n)]$, for $n = 1, 2, \ldots, N$. At every time step the sphere is rotated in such a way that its north pole is located at $[\lambda_c(t_n), \theta_c(t_n)]$. The corresponding value of ω_r is computed using Eq. (19). The velocity field is then given by Eqs. (24) and (25). More details on the algorithm are presented in the appendix.

b. Analytic solution of the transported scalar

The knowledge of the exact (analytic) solution for a given test problem is very useful for evaluating the accuracy of an advection scheme. For the moving vortex problem, we can find the exact solution at any given time. Again, we follow a two-step procedure that consists of the solid-body rotation part followed by the vortex generation. First, the vortex center $[\lambda(t_n), \theta(t_n)]$ is computed using the procedure discussed in the above section. Then the analytic vortex centered at $[\lambda_c(t_n), \theta_c(t_n)]$ with respect to $[\lambda(t_n), \theta(t_n)]$ can be computed via Eqs. (19) and (22).

c. Exact departure points for semi-Lagrangian schemes

For semi-Lagrangian schemes with backward trajectories, the upstream departure points are determined from the known velocity fields using the trajectory integrating schemes (see Staniforth and Côté 1991). However, for the moving vortex problem the exact departure points can be computed as follows. First the analytic departure points corresponding to the solid-body rotation are determined on the rotated sphere for a single time step $(\lambda' - \omega_s \Delta t, \theta')$ and then are rotated back to the regular spherical coordinates (λ_d, θ_d). The time-dependent vortex center $[\lambda_c(t_n), \theta_c(t_n)]$ can be computed as described above. In addition, the sphere needs to be rotated so that the north pole is at $[\lambda_c(t_n), \theta_c(t_n)]$ with respect to the departure coordinates (λ_d, θ_d). The upstream position for the moving vortex on the rotated sphere is then given by

$$(\lambda_d', \theta_d') = [\lambda'(\lambda_d, \theta_d) - \omega_r \Delta t, \theta'(\lambda_d, \theta_d)], \quad (26)$$

which is subsequently rotated back to the regular coordinates by employing Eqs. (10) and (11).

4. Numerical experiments

The characteristics of the moving vortex advection test is demonstrated with three very different numerical schemes. These are a discontinuous Galerkin (DG) method, a semi-Lagrangian (SL) technique, and a finite-volume (FV) scheme. The latter also employs an adaptive mesh refinement algorithm that is able to track the evolving vortices around the sphere. We focus our discussion on the versatility of the test case rather than comparing the relative advantages of the numeri-

cal methods. Nevertheless, we report the normalized ℓ_1, ℓ_2, and ℓ_∞ error norms of the transported scalar for each scheme, which are defined in W92. The corresponding definition of the error in the FV adaptive mesh application is also shown in Jablonowski et al. (2006). The error norms serve as a reference for new users of the test and are intended to foster future model intercomparisons.

a. Discontinuous Galerkin transport

The DG advection scheme developed by Nair et al. (2005) is used for the numerical simulation of the moving vortex. Since the DG scheme is based on conservation laws, we use the conservative transport equation in (14). Nair et al. (2005) employs the cubed-sphere geometry that is based on the equiangular central projection. It decomposes the sphere into six identical subdomains (faces), which results in a nonorthogonal curvilinear coordinate system that is free of singularities. Each face of the cubed sphere is further partitioned into $N_e \times N_e$ spectral elements such that $6N_e^2$ elements span the entire sphere. For the present study we used $N_e = 5$, and each spectral element has 8×8 additional Gauss–Lobatto–Legendre points [a tensor product of seventh degree polynomials; see Dennis et al. (2007) for a detailed discussion]. With this setup, there are 9600 grid points (degrees of freedom) that represent an *average* resolution of $2.6° \times 2.6°$. The DG scheme employs a time step of $\Delta t = 360$ s, which corresponds to 2880 iterations for a complete revolution around the globe. The flow orientation angle is set to $\alpha = 45°$, which translates the moving vortices across four vertices of the cubed sphere.

Figure 2 shows the evolution of the vortices in an orthographic projection such that a vortex center is kept at the center of the view angle (the other vortex forms on the diametrically opposite side and is hence invisible). Figure 2a shows the initial conditions where the contour levels vary from 0.5 to 1.5. Figures 2b–d display the evolution of the analytic solution after 3, 6, and 12 model days, respectively. Figures 2e,f show the numerical solution by the DG method after 6 and 12 days of model simulation. Note that the accuracy and efficiency of the DG method depends of the choice of N_e and the degrees of the polynomial basis function. However, the numerical details of the DG method are not the focus of our study. More information on the characteristics of the DG scheme is provided in Levy et al. (2007).

Since the analytic solution is known, the time traces of the normalized standard ℓ_1, ℓ_2, and ℓ_∞ errors sampled at every model hour are plotted in Fig. 3. The left panel shows the time traces of the errors for the flow along the equator ($\alpha = 0°$). The right panel shows the corresponding errors for the flow along the northeast direction ($\alpha = 45°$). There is a significant difference in the ℓ_∞ error growths for these two cases. For the equatorial flow case, the ℓ_∞ error growth is less oscillatory than that of the northeast flow case. This is due to the fact that the northeast flow orientation ($\alpha = 45°$) causes the deforming vortex centers to pass over four corners of the cubed sphere (weak singularities) and furthermore, move along two edges of the cubed sphere. However, for the north–south ($\alpha = 90°$) flow (not shown), the error plot looks very similar to the left panel of Fig. 3 ($\alpha = 0°$). The ℓ_1 and ℓ_2 errors are one order of magnitude smaller than the ℓ_∞ error. After one revolution, the ℓ_1 and ℓ_2 errors are 2.1×10^{-3} and 7.1×10^{-3} for $\alpha = 0$, and 1.9×10^{-3} and 6.7×10^{-3} for $\alpha = 45°$, respectively.

Note that in the cosine-bell advection problem (W92), there is no deformation involved in the flow fields. Moreover, the cosine bell only covers approximately 10% of the entire domain. Outside this small domain its value is defined to be zero. Therefore, the pattern of the ℓ_∞ error growth for the cosine-bell advection problem with identical flow orientation angles α is significantly different (see Nair et al. 2005).

b. Semi-Lagrangian advection

Semi-Lagrangian schemes are widely used in weather prediction models since they allow stable calculations with long time steps. Most often, the time steps for an SL scheme are several times longer than typical time steps permitted by the stability criterion of an Eulerian advection scheme (see Staniforth and Côté 1991). Here, we demonstrate the numerical simulation of the moving vortices with classical semi-Lagrangian advection [Eq. (15)] and employ a bicubic Lagrangian upstream interpolation scheme. Note, that the analytic departure points [Eq. (26)] are used for the upstream interpolation. The computational mesh is a regular (λ, θ) spherical grid with 73×144 (latitude $\times$ longitude) grid points. This corresponds to a uniform $2.5° \times 2.5°$ resolution that includes the two pole points. The SL advection utilizes a $\Delta t = 3600$ s time step that requires 288 iterations for a complete revolution around the globe.

Figure 4 shows the initial field and analytic solutions after 12 days in Figs. 4a,b. The SL solution for the equatorial ($\alpha = 0°$) and north–south flows ($\alpha = 90°$) after 12 days are displayed in Figs. 4c,d. The broken contour lines clearly indicate that the numerical solution does not accurately resolve the center of the vortices at the chosen resolution. Figure 5 shows the time traces of the normalized ℓ_1, ℓ_2, and ℓ_∞ error norms. The left panel ($\alpha = 0°$) exhibits a gradual error growth as
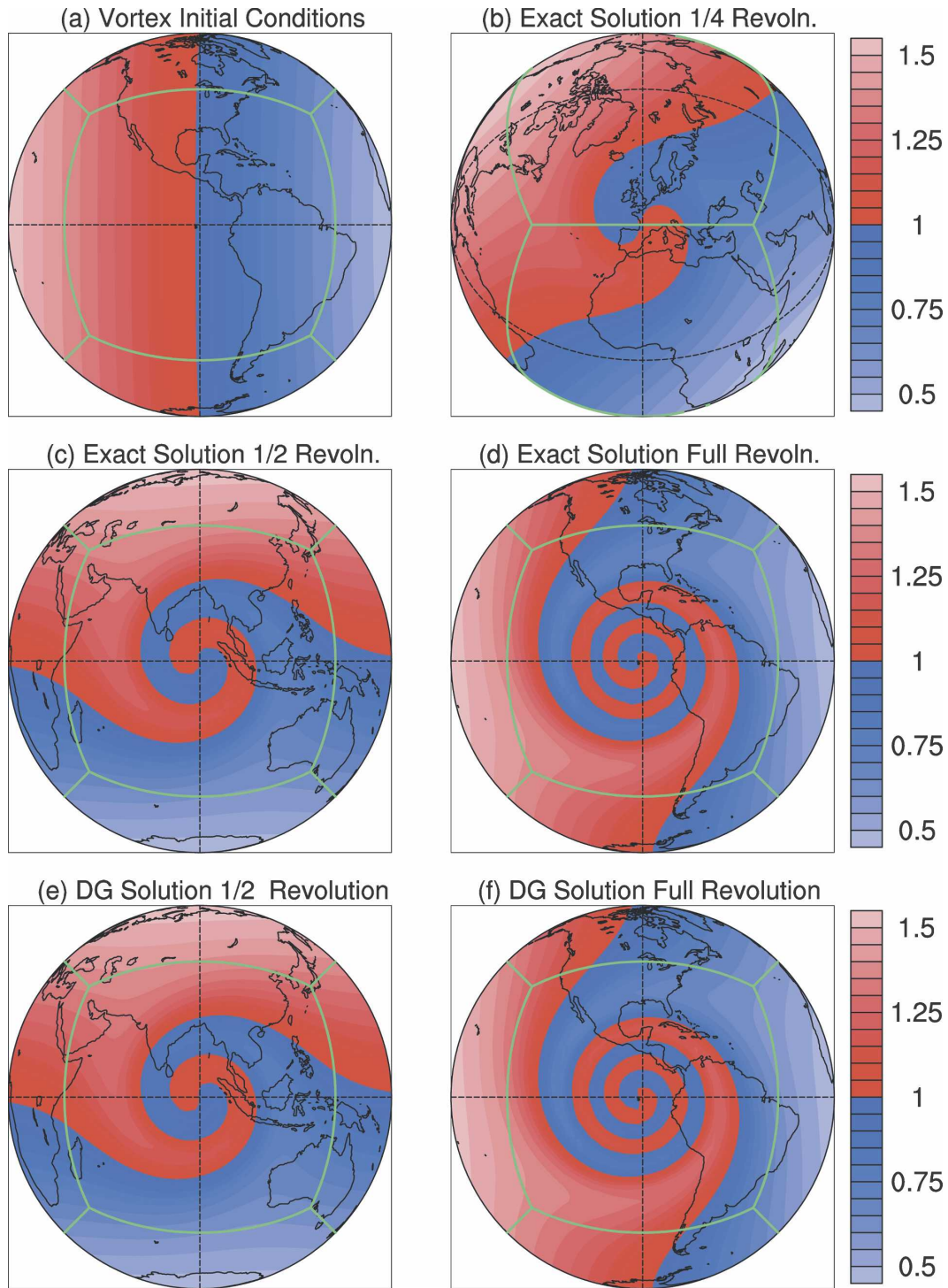
FIG. 2. Orthographic projection of the moving vortex for the rotation angle $\alpha = 45°$. (a)–(d) The exact solutions at model days 0, 3, 6, and 12 (after a full revolution). The DG solutions at (e) day 6 and (f) day 12 at the approximate resolution of $2.6° \times 2.6°$. The view angle in the figures is centered on one of the moving vortices, and the cubed-sphere geometry is used for the simulations.
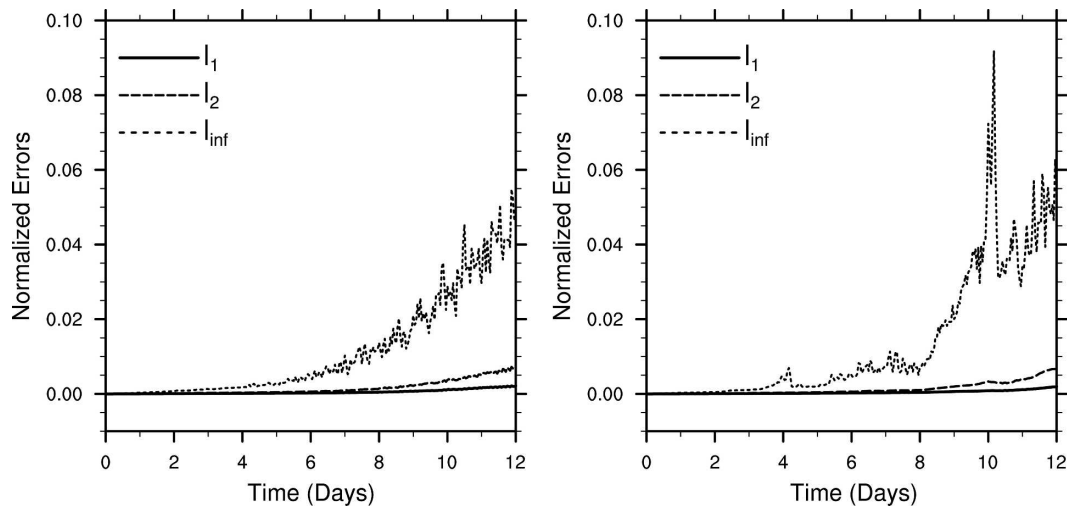
FIG. 3. Time traces of normalized standard errors ℓ_1, ℓ_2, and ℓ_∞ for a complete revolution around the globe for (left) $\alpha = 0°$ and (right) $\alpha = 45°$. The DG approach at the approximate resolution of $2.6° \times 2.6°$ is shown.

the vortices evolve and move over the equatorial regions. The right panel ($\alpha = 90°$) shows a minor jump in the error as the vortices cross the polar regions around day 3 and 9. These minor fluctuations in the error norms in polar regions are due to the polar singularities associated with the latitude–longitude grid, and not because of the particular advection scheme used or the test case itself. The cross-polar advection experiences "shocks" when crossing the two pole points. This is a typical phenomenon for many numerical discretizations with latitude–longitude grids that place grid points at the north and south poles (Nair and Machenhauer 2002). The ℓ_1 and ℓ_2 errors after one revolution are 3.7×10^{-2} and 5.7×10^{-2} for $\alpha = 0°$, and 3.6×10^{-2} and 5.4×10^{-2} for $\alpha = 90°$, respectively.

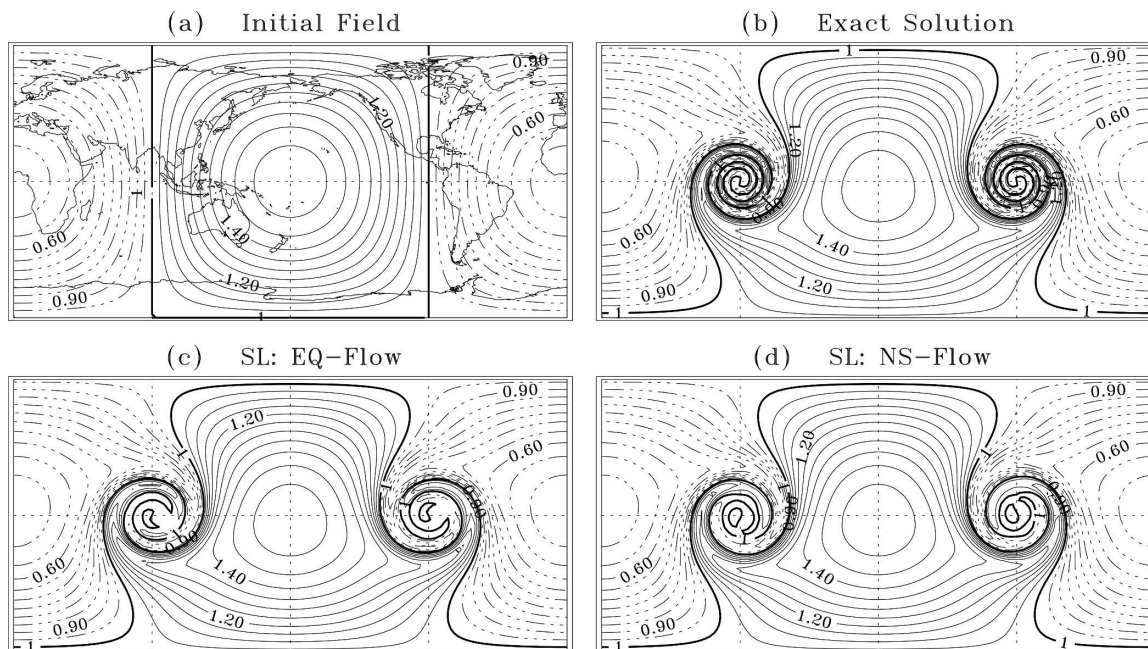As a reference, Table 1 lists the analytic solution [Eq.

FIG. 4. (a) Initial scalar field and (b) analytic solution after 12 days for the moving vortex problem. The centers of the vortices are located on the equator at 90°E initially and at 90°W after 12 days. The SL numerical solution of the scalar field for (c) $\alpha = 0°$ and (d) $\alpha = 90°$ after one full revolution (12 days). The bicubic SL advection scheme employs the latitude–longitude grid with the uniform resolution of $2.5° \times 2.5°$. The contour interval is 0.05 with dashed contours for $\phi < 1$.
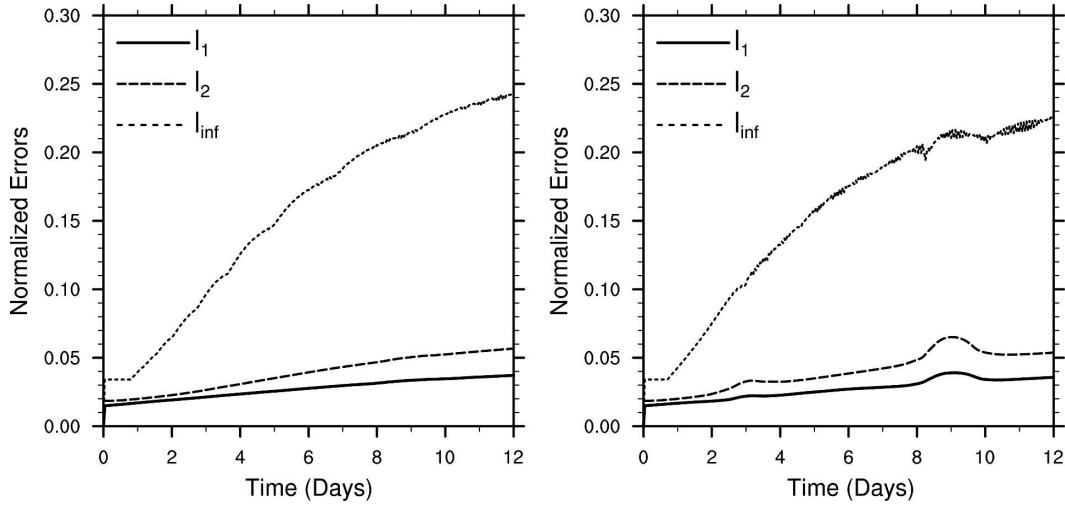
FIG. 5. Same as in Fig. 3, but for the semi-Lagrangian simulations with (left) $\alpha = 0°$ and (right) $\alpha = 90°$ on the latitude–longitude grid with a uniform resolution of 2.5°.

(22)] and departure point positions (λ_d, θ_d) in radians with respect to an arbitrarily selected grid point (λ_i, θ_j) located at (250°, 30°) as a function of time (iterations) for the flow orientation parameter $\alpha = 90°$. The selected grid point in the northern hemisphere corresponds to the longitudinal and latitudinal grid indices $(i = 101, j = 49)$ when using the previously chosen SL grid resolution (see Figs. 4c,d) with $\Delta\lambda = \Delta\theta = 2.5°$. In addition, Table 2 tabulates snapshots of the (λ_d, θ_d) departure points and analytic solutions for $\alpha = 0°$ at the alternative position $(\lambda_i, \theta_j) = (70°, -45°)$ in the southern hemisphere. This position corresponds to the grid indices $(i = 29, j = 19)$. Note that the reference grid point (λ_i, θ_j) is stationary with respect to the rotating and deforming vortex field. Furthermore, the grid index $(i = 1, j = 1)$ is located at the south pole at $(\lambda_1, \theta_1) = (0°, -90°)$ in the SL setup.

c. Finite-volume transport with AMR

To emphasize the versatility of the test we also apply the moving vortex test case to a finite-volume advection algorithm with AMR capability. The moving vortices are an ideal test candidate for AMR models, which can focus their resolution on isolated features of interest.

In recent years, AMR applications on the sphere have become more mature in atmospheric modeling [for a comprehensive review, see Behrens (2006)]. They provide an attractive framework for atmospheric flows since they allow an improved resolution in limited regions without requiring a fine grid resolution throughout the entire model domain. The model regions at high resolution are kept at a minimum and can be individually tailored toward the flow conditions. Here, a block-

structured adaptive grid technique has been applied to a revised version of the mass-conservative finite-volume advection algorithm by Lin and Rood (1996) and Lin and Rood (1997). The adaptive mesh technique is fully described in Jablonowski (2004) and Jablonowski et al. (2006). In essence, the adaptive model design utilizes the spherical adaptive-grid library by Oehmke (2004), which groups the spherical latitude–longitude grid into horizontal, logically rectangular blocks. The blocks are self-similar and split into four in the event of refinement requests, thereby doubling the spatial resolution. Coarsenings reverse this refinement principle. Then, four "children" are coalesced into a single self-similar parent block that reduces the grid resolution in each direction by a factor of 2. Neighboring blocks can only differ by one refinement level. This leads to cascading refinement regions.

For our moving vortex experiment, we start the simulation with 6 × 8 blocks on the sphere in which each

TABLE 1. The departure point position (λ_d, θ_d) and analytic solution $\phi(\lambda_i, \theta_j)$ [Eq. (22)] for the semi-Lagrangian advection with reference to a known static grid point $(\lambda_i, \theta_j) = (4.363\,323, 0.523\,599)$ radians, located at (250°, 30°) with grid indices $(i = 101, j = 49)$. The values are sampled as a function of time $t_n = n\,\Delta t$ with $\Delta t = 1$ h, and for $\alpha = 90°$.

Iteration (n)	λ_d	θ_d	$\phi(\lambda_i, \theta_j)$
1	4.369 668	0.504 552	1.174 774
48	4.364 989	0.503 785	1.229 204
96	4.367 290	0.503 051	1.185 997
144	4.365 472	0.501 753	1.292 421
192	4.370 011	0.502 384	0.902 104
240	4.367 708	0.503 113	1.150 744

TABLE 2. Same as in Table 1, but for $\alpha = 0°$ and $(\lambda_i, \theta_j) = (1.221\ 731, -0.785\ 398)$ located at $(70°, -45°)$ with grid indices $(i = 29, j = 19)$.

Iteration (n)	λ_d	θ_d	$\phi\ (\lambda_i, \theta_j)$
1	1.200 855	−0.785 787	0.847 869
48	1.199 943	−0.785 589	0.608 289
96	1.199 452	−0.785 768	0.755 740
144	1.198 931	−0.785 015	1.206 699
192	1.199 884	−0.785 208	1.408 196
240	1.200 375	−0.785 028	1.316 348

block contains 6×9 grid points in the latitudinal and longitudinal directions, respectively. This initial setup corresponds to a coarse $5° \times 5°$ uniform mesh. The variables u, v, and ϕ are positioned on a staggered Arakawa C grid (Arakawa and Lamb 1977). This places the scalar points at the centers of the finite volumes whereas the velocities are located at the midpoints of the surrounding cell edges. Note that the two pole points are v velocity points. No scalars are assigned to the poles. The FV advection model is initialized with gridpoint values. During the simulation though, cell-averaged values of ϕ are predicted while utilizing time-centered velocities. These gridpoint velocities are evaluated analytically at the discrete half-time levels $t_{n+1/2} = (n + ½)\Delta t$ using Eqs. (24) and (25).

The adaptive refinements are guided by a gradient criterion. In particular, refinements up to the maximum refinement level of 3 are invoked if the magnitude of the gradient is $|a\nabla\phi| \geq 1$. This leads to the minimum grid resolution $0.625° \times 0.625°$ in the refined blocks. Coarsenings, on the other hand, are applied if the criterion is no longer fulfilled (e.g., after the moving vortex with its sharp gradients left a refined domain). Here, we do not actively refine the blocks closest to the poles in order to allow larger time steps. Any adaptations at the poles are only triggered by the refinement cascade.

Snapshots of the adaptive grid simulation with rotation angle $\alpha = 45°$ at days 3, 6, 9, and 12 are shown in Fig. 6. It can clearly be seen that the adaptive blocks (Figs. 6e–h) successfully track the evolving vortices (Figs. 6a–d). Note that the initial scalar field is smooth. The gradient then sharpens gradually during the course of the simulation. As a consequence, the refinement criterion is not fulfilled before day 2, which leads to slightly increased error levels due to the coarse initial $5° \times 5°$ resolution. After day 2, the adaptations slow down the error growth. This behavior is shown in Fig. 7, which displays the time traces of several ℓ_2 and ℓ_∞ error norms for both uniform and adapted runs with the alternative flow orientation angle $\alpha = 0°$. Here the errors

of the adaptive runs with 1, 2, and 3 refinement levels are compared to the corresponding uniform-resolution simulations with the same model. The adaptive mesh experiments successfully flatten the increased error levels shortly after day 2 when the first adaptations are introduced. At day 12 the adaptive runs match rather well, or are even lower than, the error norms of the fixed-resolution runs at the various resolutions. This is also shown in Table 3, which lists the normalized ℓ_1, ℓ_2, and ℓ_∞ error norms as well as time step statistics for the adapted and uniform grid model runs after 12 days. The lower AMR error norms are mostly due to the fact that the adaptive simulations require fewer time steps to complete one full revolution. Note that the time step in the adapted runs is variable and matches a Courant–Friedrichs–Lewy (CFL) stability criterion of $|CFL| \leq 0.95$. In contrast, the time steps in the uniform-resolution runs are held constant and guarantee $\max|CFL| \leq 0.9$. In particular, the maximum CFL numbers of the uniform-grid FV runs are 0.66, 0.69, 0.89, and 0.85 for the grid resolutions $5° \times 5°$, $2.5° \times 2.5°$, $1.25° \times 1.25°$, and $0.625° \times 0.625°$, respectively. The reduced number of time steps in the adaptive runs is attributable to the fact that longer time steps can be used if the refined grid does not cover the polar region. Near the poles, the CFL condition is most restrictive because of the convergence of the meridians in the chosen spherical grid [also see the discussion by Hubbard and Nikiforakis (2003)].

As implied by Table 3, the FV advection algorithm converges steadily toward the analytic solution. The convergence rate for the moving vortex problem lies between second and first order, which is below the design order of the numerical scheme. A similar FV convergence rate was also observed for the stationary vortex problem, whereas the convergence rate for the pure solid-body rotation lies around the second order [see tables in Jablonowski et al. (2006)]. The reduction in the expected rate is due to the nonsmooth nature of the vortex test case with two singular points at the vortex centers.

5. Conclusions

A new 2D test case for the advection (transport) problem on the sphere is developed. The test consists of components from the deformational flow (Nair and Machenhauer 2002) and the standard solid-body rotation test. The flow field is time dependent and deformational and can be oriented as in the case of the standard solid-body rotation test considered in W92. The test introduces two moving vortices that are centered at diametrically opposite sides of the sphere and move
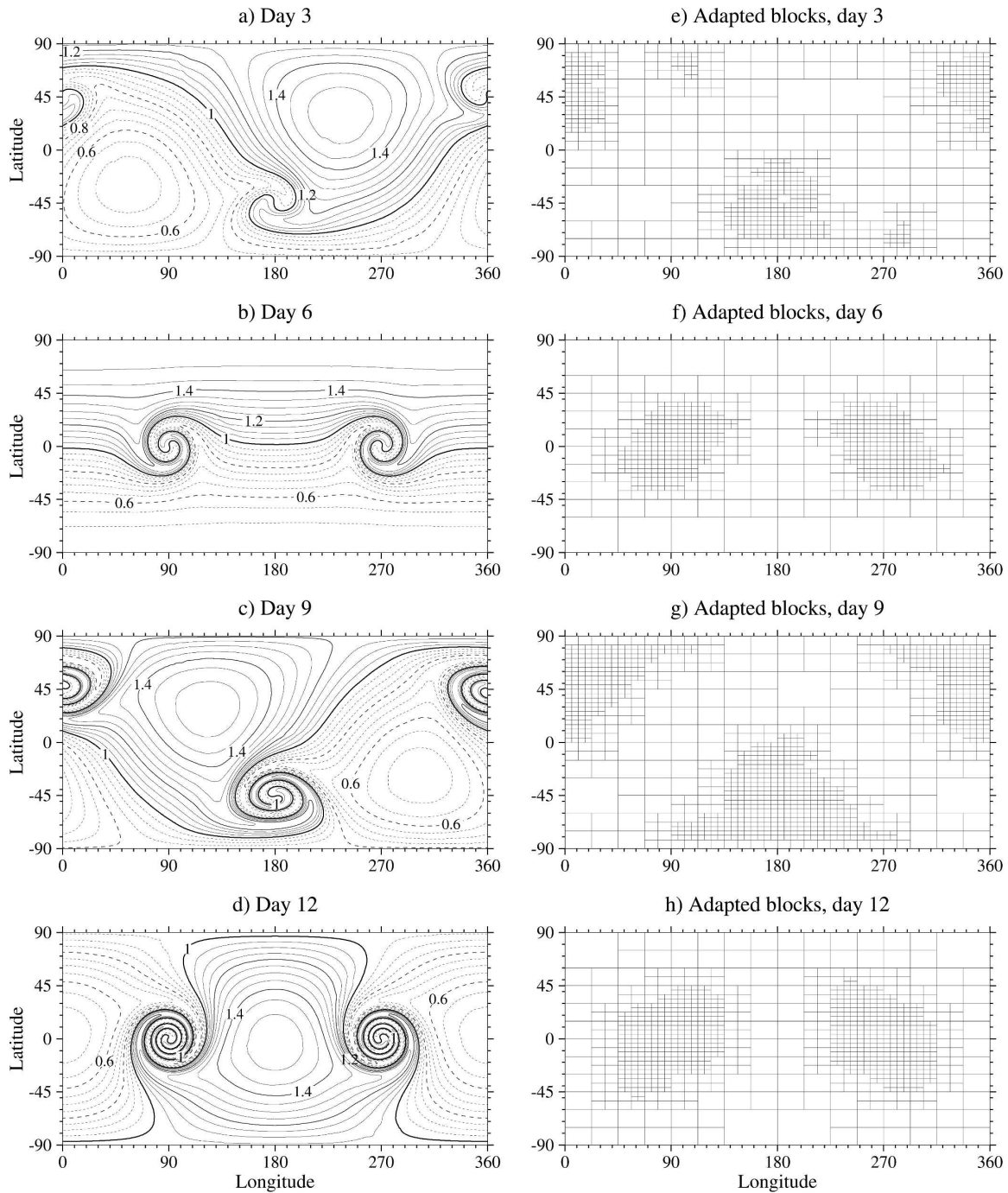
FIG. 6. Snapshots of the moving vortices with $\alpha = 45°$ at days 3, 6, 9, and 12 (after one full revolution) computed with the adaptive grid version of the FV advection model with three refinement levels (coarsest resolution is $5° \times 5°$, finest is $0.625° \times 0.625°$). (a)–(d) Advected scalar field ϕ with contour interval 0.05; contours for $\phi < 1$ are dashed. (e)–(h) Corresponding adapted blocks; each block consists of 6×9 grid points in lat $\times$ lon direction (grid points not shown). The refinement criterion tracks regions with $|a\nabla\phi| \geq 1$.

along a predetermined great circle trajectory with a known analytic solution. The wind field is nondivergent and time dependent. The rotational parameters are scaled in such a way that 12 days are required to com-

plete a full revolution around the globe. This test is far more challenging than the existing advection test cases on the sphere. An algorithm for generating the vortices as a function of the flow orientation parameter α and
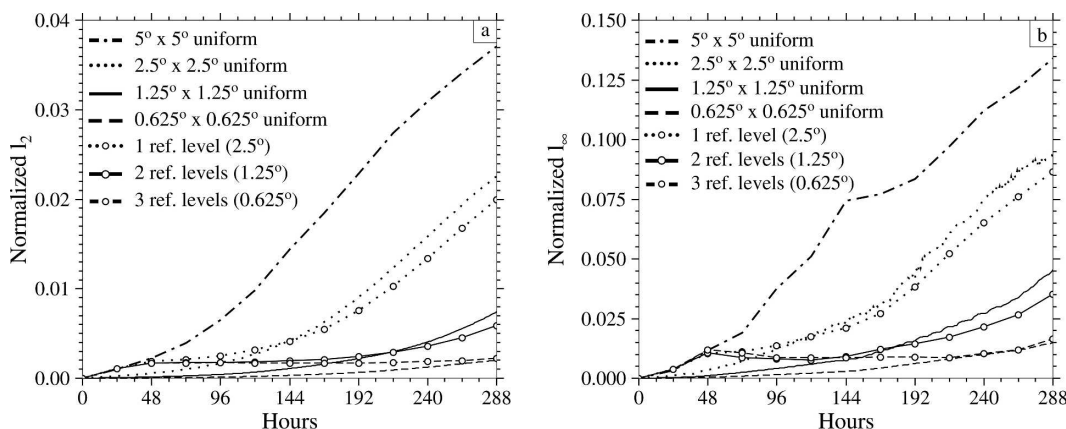
FIG. 7. Time traces of the normalized (a) ℓ_2 and (b) ℓ_∞ error norms for the moving vortex test with $\alpha = 0°$. The adaptive FV simulations with 1, 2, and 3 refinement levels are compared with the corresponding uniform-resolution FV runs.

time is described. In addition, an algorithm for determining the analytic departure points for semi-Lagrangian models is provided. Since the analytic solution is known, the time traces of the normalized ℓ_1, ℓ_2, and ℓ_∞ errors can be immediately computed. Here, time traces of the errors for flows along the equatorial, northeast or north–south direction have been assessed.

The characteristics and versatility of the test have been demonstrated with three different advection schemes that vary in complexity. Among them were a conservative discontinuous Galerkin method on a cubed-sphere grid and a classical (nonconservative) semi-Lagrangian advection scheme that employed a bicubic Lagrangian upstream interpolation on a latitude–longitude mesh. In addition, we tested the moving vortices in an adaptive mesh application that utilized the conservative finite-volume advection algorithm by Lin and Rood (1997) in latitude–longitude geometry. This adaptive experiment showed that the vortices can be successfully tracked by high-resolution grids when using a gradient-based adaptation criterion. The re-fined grid then follows the moving vortices and detects the slowly increasing magnitude of the scalar gradient. This approach considerably slows down the growth of the error norms and closely matches the solutions of uniform-mesh simulations.

In general, all three advection schemes reliably simulated the evolving flow field. Different characteristics of the numerical approaches were demonstrated by various normalized error norms, although they were not the focus of the discussion. The purpose of the application examples is to provide a basis for future model intercomparisons.

The proposed test problem provides a challenging test case with a known analytic solution for global transport schemes. Because of the nonlocalized evolving nature of the advecting field, this test is an ideal candidate for testing advection schemes with adaptive mesh refinement capability. The moving vortex test case complements the existing advection tests for horizontal flows in spherical geometry. We will be happy to make the vortex code for the initial conditions and reference solutions available to interested users.

TABLE 3. Error measures and time step statistics for the FV simulations with $\alpha = 0°$ after 12 days. Model runs with different refinement levels and uniform-grid simulations are compared and grouped together according to their finest grid resolution. The CFL number for the adapted runs is 0.95 (variable time step).

Base resolution $\Delta\lambda$, $\Delta\theta$	Refinement level	Error norms			Time step Δt(s)	No. of time steps
		$\ell_1(\phi)$	$\ell_2(\phi)$	$\ell_\infty(\phi)$		
5°	0	0.0165	0.0371	0.1341	7200	144
2.5°	0	0.0078	0.0226	0.0947	3600	288
5°	1	0.0077	0.0200	0.0865	Variable	193
1.25°	0	0.0022	0.0074	0.0454	1800	576
5°	2	0.0026	0.0059	0.0353	Variable	372
0.625°	0	0.0005	0.0020	0.0149	600	1728
5°	3	0.0014	0.0022	0.0164	Variable	730

APPENDIX

Reference Solution for the Moving Vortex Test Case

The moving vortex problem involves a back-and-forth rotation of the sphere via Eqs. (8)–(11). Inverting the trigonometric functions, particularly for λ and λ' [Eqs. (8) and (10)], can be problematic because of the nonunique nature of the inverted (arctan) function values. To avoid this problem we recommend using the intrinsic FORTRAN function atan2(y, x) for arctan(y/x), which provides values in the range $[-\pi, \pi]$. The negative values between $[-\pi, 0]$ then need to be *shifted* by adding 2π. This guarantees the proper branch will be cut in the longitudinal direction between $[0, 2\pi]$.

The analytic solution is generated at the equator of a rotated sphere. As described in section 3 this procedure involves multiple rotations of the sphere. However, to ease the computations, we recommend the following approach where the vortex center reaches a known fixed position at any given time t_n. This may be interpreted as if the vortex center originates from an upstream position and reaches a known position (λ_c, θ_c) at time t_n. This provides a reliable way to track the center. The computational procedure for the analytic solution is as follows:

- Rotate a sphere such that its north pole is located at $(\lambda_p, \theta_p) = (\pi, \pi/2 - \alpha)$ with respect to the regular (λ, θ) sphere. The rotated coordinate system is (λ', θ') and is computed using Eqs. (8) and (9).
- Move the (λ', θ') coordinates to the "upstream position" using the solid-body rotation angular velocity (ω_s) with respect to the fixed north pole $(\pi, \pi/2 - \alpha)$ position [i.e., $(\lambda'_s, \theta'_s) \leftarrow (\lambda' - \omega_s t_n, \theta' - 0)$]. Rotate (λ'_s, θ'_s) back to the regular coordinates (λ_s, θ_s) by employing Eqs. (10) and (11).
- Generate the analytic vortex with center at (λ_c, θ_c) with respect to the (λ_s, θ_s) sphere using Eq. (22). This step involves rotating the (λ_s, θ_s) sphere such that the rotated sphere has the north pole at the vortex center.

REFERENCES

Arakawa, A., and V. R. Lamb, 1977: Computational design of the basic dynamical process of the UCLA general circulation model. *Methods in Computational Physics,* J. Chang, Ed., Academic Press, 173–265.

Behrens, J., 2006: *Adaptive Atmospheric Modeling—Key Techniques in Grid Generation, Data Structures, and Numerical Operations with Applications*. Lecture Notes in Computational Science and Engineering, Vol. 54, Springer, 214 pp.

Dennis, J., R. D. Nair, H. M. Tufo, M. Levy, and T. Voran, 2007: Development of a scalable global discontinuous Galerkin atmospheric model. *Int. J. Comput. Sci. Eng.,* in press.

Doswell, C. A., 1984: A kinematic analysis associated with a non-divergent flow. *J. Atmos. Sci.,* **41,** 1242–1248.

Flyer, N., and G. B. Wright, 2007: Transport schemes on a sphere using radial basis functions. *J. Comput. Phys.,* **226,** 1059–1084.

Hubbard, M. E., and N. Nikiforakis, 2003: A three-dimensional, adaptive, Godunovtype model for global atmospheric flows. *Mon. Wea. Rev.,* **131,** 1848–1864.

Jablonowski, C., 2004: Adaptive grids in weather and climate modeling. Ph.D. dissertation, Department of Atmospheric, Oceanic and Space Sciences, University of Michigan, 292 pp.

——, M. Herzog, J. E. Penner, R. C. Oehmke, Q. F. Stout, B. van Leer, and K. G. Powell, 2006: Block-structured adaptive grids on the sphere: Advection experiments. *Mon. Wea. Rev.,* **134,** 3691–3713.

Levy, M. N., R. D. Nair, and H. M. Tufo, 2007: High-order Galerkin method for scalable global atmospheric models. *Comput. Geosci.,* **124,** 1022–1035.

Lin, S.-J., and R. B. Rood, 1996: Multidimensional flux-form semi-Lagrangian transport scheme. *Mon. Wea. Rev.,* **124,** 2046–2070.

——, and ——, 1997: An explicit flux-form semi-Lagrangian shallow water model on the sphere. *Quart. J. Roy. Meteor. Soc.,* **123,** 2477–2498.

Lipscomb, W. H., and T. D. Ringler, 2005: An incremental remapping transport scheme on a spherical geodesic grid. *Mon. Wea. Rev.,* **133,** 2335–2350.

Nair, R. D., and B. Machenhauer, 2002: The mass-conservative cell-integrated semi-Lagrangian advection scheme on the sphere. *Mon. Wea. Rev.,* **130,** 649–667.

——, J. Côté, and A. Staniforth, 1999: Cascade interpolation for semi-Lagrangian advection over the sphere. *Quart. J. Roy. Meteor. Soc.,* **125,** 1445–1468.

——, J. S. Scroggs, and F. H. M. Semazzi, 2003: A forward-trajectory global semi-Lagrangian transport scheme. *J. Comput. Phys.,* **190,** 275–294.

——, S. J. Thomas, and R. D. Loft, 2005: A discontinuous Galerkin transport scheme on the cubed-sphere. *Mon. Wea. Rev.,* **133,** 814–828.

Oehmke, R. C., 2004: High performance dynamic array structures. Ph.D. dissertation, Department of Electrical Engineering and Computer Science, University of Michigan, 93 pp.

Peng, X., F. Xiao, and K. Takahashi, 2006: Conservative constraint for a quasi-uniform overset grid on the sphere. *Quart. J. Roy. Meteor. Soc.,* **132,** 979–996.

Ritchie, H., 1987: Semi-Lagrangian advection on a Gaussian grid. *Mon. Wea. Rev.,* **115,** 608–619.

Staniforth, A., and J. Côté, 1991: Semi-Lagrangian integration schemes for atmospheric modeling—A review. *Mon. Wea. Rev.,* **119,** 2206–2223.

Williamson, D. L., and P. J. Rasch, 1989: Two-dimensional semi-Lagrangian transport with shape-preserving interpolation. *Mon. Wea. Rev.,* **117,** 102–129.

——, J. B. Drake, J. J. Hack, R. Jakob, and P. N. Swarztrauber, 1992: A standard test set for numerical approximations to the shallow water equations in spherical geometry. *J. Comput. Phys.,* **102,** 211–224.

Zerroukat, M., N. Wood, and A. Staniforth, 2004: "SLICE" A semi-Lagrangian inherently conservative and efficient transport scheme for transport problems on the sphere. *Quart. J. Roy. Meteor. Soc.,* **130,** 2649–2664.